

Deterministic entanglement of ions in thermal states of motion

G Kirchmair^{1,2}, J Benhelm^{1,2}, F Zähringer^{1,2}, R Gerritsma^{1,2},
C F Roos^{1,2} and R Blatt^{1,2}

¹Institut für Quantenoptik und Quanteninformation, Österreichische Akademie der Wissenschaften, Otto-Hittmair-Platz 1, A-6020 Innsbruck, Austria

²Institut für Experimentalphysik, Universität Innsbruck, Technikerstr. 25, A-6020 Innsbruck, Austria

E-mail: Christian.Roos@uibk.ac.at

Abstract. We give a detailed description of the implementation of a Mølmer-Sørensen gate entangling two $^{40}\text{Ca}^+$ ions using a bichromatic laser beam near-resonant with a quadrupole transition. By amplitude pulse shaping and compensation of AC-Stark shifts we achieve a fast gate operation without compromising the error rate. Subjecting different input states to concatenations of up to 21 individual gate operations reveals Bell state fidelities above 0.80. In principle, the entangling gate does not require ground state cooling of the ions as long as the Lamb-Dicke criterion is fulfilled. We present the first experimental evidence for this claim and create Bell states with a fidelity of 0.974(1) for ions in a thermal state of motion with a mean phonon number of $\bar{n} = 20(2)$ in the mode coupling to the ions' internal states.

Submitted to: *New J. Phys.*

1. Introduction

Building a device that is able to carry out arbitrary calculations by exploiting the laws of quantum physics has been an experimental challenge for more than a decade now. A large variety of physical implementations have been conceived to meet the requirements for quantum information processing summarized in [1]. Among these implementations, strings of ions stored in linear Paul traps and manipulated by laser pulses have proven to be a particularly successful architecture to realize quantum information processing. Experiments with trapped ions have shown long relevant coherence times [2, 3, 4], the ability to faithfully initialize and read-out qubits [5, 6] and high fidelity quantum operations [7, 8, 9]. Current efforts are focussed on scaling up ion trap experiments to handle many ions, improving the quality and speed of the basic operations and integrating the various techniques into a single system. Concerning the basic operations, the realization of universal multi-qubit gates is particularly challenging. Many different types of gates have been proposed over the last years and several of them have been

experimentally investigated. Gates using a collective interaction [8, 10] between the ions and the laser field - until recently only applied to qubits encoded in the hyperfine structure (hyperfine qubits) - were very successful in creating multi-particle entangled states and demonstrating simple quantum error correction techniques [11].

Recently we demonstrated the first application of a Mølmer-Sørensen gate operation to an optical qubit, i.e. a qubit encoded in a ground and a metastable state of $^{40}\text{Ca}^+$ ions, deterministically creating Bell states with a so far unmatched fidelity of 0.993(1) [9]. Here, we present a further investigation of this universal gate operation acting on optical qubits and extend the theoretical and experimental analysis. Particular emphasis is put on the compensation of AC-Stark shifts and amplitude pulse shaping to reach high fidelities without compromising the gate speed substantially. The gate characterization is extended further by investigating the fidelity decay for different input states after up to 21 individual operations.

Moreover, we report on the first experiments demonstrating a universal entangling gate operating on Doppler-cooled ions. We derive simple expressions [12] for the qubit populations under the action of the gate and use these equations to infer the mean vibrational quantum number \bar{n} of the axial center-of-mass mode. For ions in a thermal state with $\bar{n} = 20(2)$, we obtain Bell states with a fidelity of 0.974(1).

The ability to implement high fidelity multi-qubit operations on Doppler-cooled ions is of practical interest in ion trap quantum information processing as the implementation of quantum algorithms demands several techniques that do not conserve the ions' vibrational quantum state: (i) State detection of ancilla qubits as required by quantum error correction schemes [13] can excite the ion string to a thermal motional state close to the Doppler limit because of the interaction with the laser inducing the ions to fluoresce. (ii) Experiments with segmented traps structures where ion strings are split into smaller strings also tend to heat up the ions slightly [14]. Here, the availability of high-fidelity gate operations even for thermal states may provide a viable alternative to the technically involved re-cooling techniques using a different ion species [15, 16].

2. Theoretical gate description

2.1. Mølmer-Sørensen gate

A two-qubit quantum gate that is equivalent to a controlled-NOT gate up to local operations is achieved by the action of a Hamiltonian $H \propto \sigma_n \otimes \sigma_n$, where $\sigma_n = \sigma \cdot \mathbf{n}$ is a projection of the vector of Pauli spin matrices onto the direction \mathbf{n} [17]. Two prominent examples of this type of gate are the conditional phase gate [8, 18] and the Mølmer-Sørensen gate [19, 20, 10]. In the latter case, correlated spin flips between the states $|\uparrow\rangle|\uparrow\rangle \leftrightarrow |\downarrow\rangle|\downarrow\rangle$ and $|\uparrow\rangle|\downarrow\rangle \leftrightarrow |\downarrow\rangle|\uparrow\rangle$ are induced by a Hamiltonian

$$H \propto \sigma_\phi \otimes \sigma_\phi \quad \text{where} \quad \sigma_\phi = \cos \phi \sigma_x + \sin \phi \sigma_y. \quad (1)$$

The unitary operation $U = \exp(i\frac{\pi}{4}\sigma_\phi \otimes \sigma_\phi)$ maps product states onto maximally entangled states. In 1999, the proposal was made to realize an effective Hamiltonian [19,

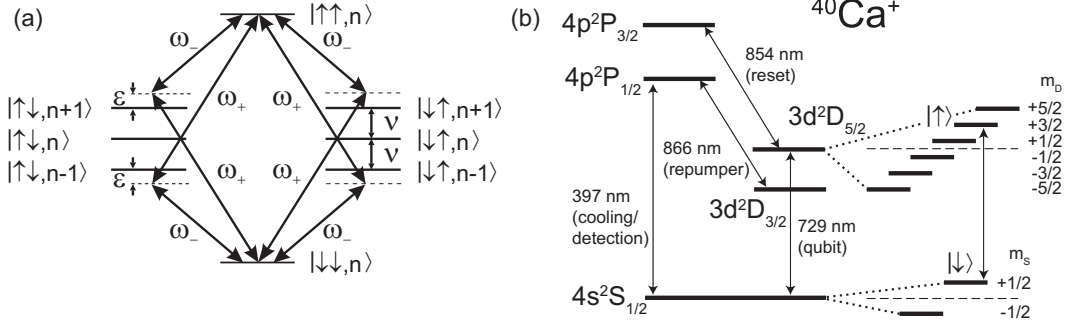


Figure 1. (a) Mølmer-Sørensen interaction scheme. A bichromatic laser field couples the qubit states $|\downarrow\downarrow\rangle \leftrightarrow |\uparrow\uparrow\rangle$ via the four interfering paths shown in the figure. Similar processes couple the states $|\uparrow\downarrow\rangle \leftrightarrow |\downarrow\uparrow\rangle$. The frequencies ω_{\pm} of the laser field are tuned close to the red and the blue motional sidebands of the qubit transition with frequency ω_0 , and satisfy the resonance condition $2\omega_0 = \omega_+ + \omega_-$. The vibrational quantum number is denoted n . (b) Level scheme of $^{40}\text{Ca}^+$ showing the transitions used for cooling/detecting, repumping and resetting the state of the ion as well as the qubit transition. The qubit is encoded in the metastable state $|\uparrow\rangle = |D_{5/2}, m = 3/2\rangle$ and the ground state $|\downarrow\rangle = |S_{1/2}, m = 1/2\rangle$.

20] taking the form (1) by exciting both ions simultaneously with a bichromatic laser beam with frequencies $\omega_{\pm} = \omega_0 \pm \delta$ where ω_0 is the qubit transition frequency and δ is close to a vibrational mode of the two-ion crystal with frequency ν (see figure 1(a)). Changing into an interaction picture and performing a rotating-wave approximation, the time-dependent Hamiltonian

$$H(t) = \hbar\Omega(e^{-i\delta t} + e^{i\delta t})e^{i\eta(ae^{-i\nu t} + a^\dagger e^{i\nu t})}(\sigma_+^{(1)} + \sigma_+^{(2)}) + \text{h.c.} \quad (2)$$

is well approximated by

$$H(t) = -\hbar\eta\Omega(a^\dagger e^{i(\nu-\delta)t} + ae^{-i(\nu-\delta)t})S_y \quad (3)$$

in the Lamb-Dicke regime where the Lamb-Dicke factor η satisfies the condition $\eta \ll 1$. In (3), we use a collective spin operator $S_y = \sigma_y^{(1)} + \sigma_y^{(2)}$ and denote the laser detuning from the motional sidebands by $\nu - \delta = \epsilon$. The Rabi frequency on the carrier transition is denoted Ω , and a, a^\dagger are the phonon annihilation and creation operators, respectively. This Hamiltonian can be exactly integrated [21] yielding the propagator

$$U(t) = \hat{D}(\alpha(t)S_y) \exp(i(\lambda t - \chi \sin(\epsilon t))S_y^2), \quad (4)$$

where $\alpha(t) = \frac{\eta\Omega}{\epsilon}(e^{i\epsilon t} - 1)$, $\lambda = \eta^2\Omega^2/\epsilon$, $\chi = \eta^2\Omega^2/\epsilon^2$, and $\hat{D}(\alpha) = e^{\alpha a^\dagger - \alpha^* a}$ is a displacement operator. For a gate time $t_{\text{gate}} = 2\pi/|\epsilon|$, the displacement operator vanishes so that the propagator $U(t_{\text{gate}}) = \exp(i\lambda t_{\text{gate}}S_y^2)$ can be regarded as being the action of an effective Hamiltonian

$$H_{\text{eff}} = -\hbar\lambda S_y^2 = -2\hbar\lambda(\mathbb{1} + \sigma_y \otimes \sigma_y) \quad (5)$$

taking on the form given in (1). Setting $\Omega = |\epsilon|/(4\eta)$, a gate is realized capable of maximally entangling ions irrespective of their motional state. In the description of the gate mechanism given so far, a coupling of the light field to the carrier transition was

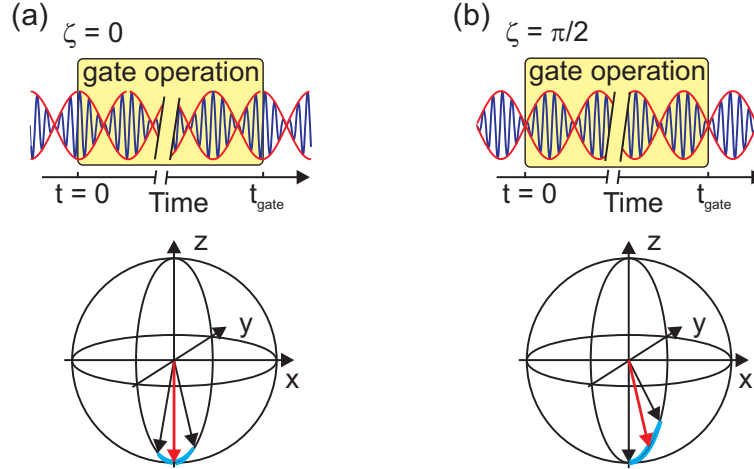


Figure 2. Effect of non-resonant excitation of the carrier transition. (a) For $\zeta = 0$, the gate starts at a maximum of the intensity-modulated beam. In this case, a Bloch vector initially centered at the south pole of the Bloch sphere performs oscillations that are symmetric around the initial position. (b) For $\zeta = \pi/2$, the gate starts at the minimum of the intensity modulation. In this case, the average orientation of the Bloch vector is tilted with respect to its initial position.

neglected based on the assumption that the Rabi frequency Ω was small compared to the detuning δ of the laser frequency components from the transition. In this case, small non-resonant Rabi oscillations that appear on top of the gate dynamics are the main effect of coupling to the carrier transition. Since a maximally entangling gate requires a Rabi frequency $\Omega \propto \eta^{-1} t_{\text{gate}}^{-1}$, the question of whether $\Omega \ll \delta$ holds becomes crucial in the limit of fast gate operations and small Lamb-Dicke factors. Our experiments [9] are exactly operating in this regime, and it turns out that non-resonant excitation of the carrier transition has further effects beyond inducing non-resonant oscillations [12]. This becomes apparent by interpreting terms in the Hamiltonian in a different way: The red- and blue-detuned frequency components $E_{\pm} = E_0 \cos((\omega_0 \pm \delta)t \pm \zeta)$ of equal intensity may be viewed as a single laser beam $E(t) = E_+ + E_- = 2E_0 \cos(\omega_0 t) \cos(\delta t + \zeta)$ that is resonant with the qubit transition but amplitude-modulated with frequency δ . Here, the phase ϕ which determines whether the gate operation starts in a maximum ($\zeta = 0$) or a minimum ($\zeta = \pi/2$) of the intensity of the amplitude-modulated beam has a crucial influence on the gate. This can be intuitively understood by considering the initial action the gate exerts on an input state in the Bloch sphere picture shown in figure 2. For short times, coupling to the sidebands can be neglected which justifies the use of a single-ion picture. The dynamics is essentially the one of two uncoupled qubits. The fast dynamics of the gate is induced by excitation of the ions on the carrier transition. For $\zeta = 0$, the Bloch vector of an ion initially in state $|\downarrow\rangle$ will oscillate with frequency δ along a line centered on the south pole of the Bloch sphere. For $\zeta = \pi/2$, the oscillation frequency is the same, however, the time-averaged position of the Bloch

vector is tilted by an angle

$$\psi = \frac{4\Omega}{\delta} \sin \zeta \quad (6)$$

with respect to the initial state $|\downarrow\rangle$. This effect has a profound influence on the gate action. A careful analysis of the gate mechanism [12] taking into account the non-resonant oscillations reveals that the Hamiltonian (3) is changed into

$$H(t) = -\hbar\eta\Omega(a^\dagger e^{i(\nu-\delta)t} + ae^{-i(\nu-\delta)t})S_{y,\psi}, \quad (7)$$

where

$$S_{y,\psi} = S_y \cos \psi + S_z \sin \psi, \quad (8)$$

and that the propagator (4) needs to be replaced by

$$U(t) = \exp(-iF(t)S_x)\hat{D}(\alpha(t)S_{y,\psi})\exp(i(\lambda t - \chi \sin(\epsilon t))S_{y,\psi}^2), \quad (9)$$

where the term containing $F(t) = \frac{2\Omega}{\delta}(\sin(\delta t + \zeta) - \sin \zeta)$ describes non-resonant excitation of the carrier transition. The dependence of the propagator on the exact value of ζ is inconvenient from an experimental point of view. To realize the desired gate, precise control over ζ is required. In addition, the gate duration must be controlled to better than a fraction of the mode oscillation period because of the non-resonant oscillation. Fortunately, both of these problems can be overcome by shaping the overall intensity of the laser pulse such that the Rabi frequency $\Omega(t)$ smoothly rises within a few cycles $2\pi/\delta$ to its maximum value $\Omega_{\text{gate}} \approx |\epsilon|/(4\eta)$ and smoothly falls off to zero at the end of the gate. In this case, the non-resonant oscillations vanish and (6) shows that the operator $S_{y,\psi}(t)$ adiabatically follows the laser intensity so that it starts and ends as the desired operator S_y irrespective of the phase ζ . For intensity-shaped pulses, the propagator (4) provides therefore an adequate description of the gate action.

2.2. AC-Stark shifts

In the description of the gate mechanism given so far the ion was treated as an ideal two-level system. AC-Stark shifts are completely insignificant provided that the intensities of the blue- and the red-detuned frequency components are the same since in this case light shifts of the carrier transition caused by the blue-detuned part are exactly canceled by light shifts of the red-detuned light field. Similarly, light shifts of the blue-detuned frequency component non-resonantly exciting the upper motional sideband are perfectly canceled by light shifts of the red-detuned frequency component coupling to the lower motional sideband.

For an experimental implementation with calcium ions, we need to consider numerous energy levels (see figure 1(b)). Here, the laser field inducing the gate action causes AC-Stark shifts on the qubit transition frequency due to non-resonant excitation of far-detuned dipole transitions and also of other $S_{1/2} \leftrightarrow D_{5/2}$ Zeeman transitions. The main contributions arise from couplings between the qubit states and the $4p$ -states that are mediated by the dipole transitions $S_{1/2} \leftrightarrow P_{1/2}$, $S_{1/2} \leftrightarrow P_{3/2}$, $D_{5/2} \leftrightarrow P_{3/2}$.

Other transitions hardly matter as can be checked by comparing the experimental results obtained in [22] with numerical results based on the transition strengths [23] of the dipole transitions coupling to the $4p$ -states. For suitably chosen k -vector and polarization of the bichromatic laser beam, these shifts are considerably smaller than the strength λ of the gate interaction.

AC-Stark shifts can be compensated for by a suitable detuning of the gate laser. An alternative strategy consists in introducing an additional AC-Stark shift of opposite sign that is also caused by the gate laser beam [22]. This approach has the advantage of making the AC-Stark compensation independent of the gate laser intensity. In contrast to previous gates relying on this technique [24] where the AC-Stark shift was caused by the quadrupole transition and compensated by coupling to dipole transitions, here, the AC-Stark shift is due to dipole transitions and needs to be compensated by coupling to the quadrupole transition.

For ions prepared in the ground state of motion ($n = 0$), a convenient way of accomplishing this task is to perform the gate operation with slightly imbalanced intensities of the blue- and the red-detuned laser frequency components. Setting the Rabi frequency of the blue-detuned component to $\Omega_b = \Omega(1 + \xi)$ and the one of the red-detuned to $\Omega_r = \Omega(1 - \xi)$, an additional light shift caused by coupling to the carrier transition is induced that amounts to $\delta_{ac}^{(C)} = 2(\Omega_r^2 - \Omega_b^2)/\delta = -8\Omega^2\xi/\delta$. Now, the beam imbalance parameter ξ needs to be set such that the additional light shift exactly cancels the phase shift $\phi = \delta_{ac}t_{gate}$ induced by the dipole transitions during the action of the gate. Taking into account that $t_{gate} = 2\pi/\epsilon$ and $\Omega = |\epsilon|/(4\eta)$, this requires $\xi = (\delta\eta^2/|\epsilon|)(\phi/\pi)$.

Apart from introducing light shifts, setting $\xi \neq 0$ also slightly changes the gate Hamiltonian (5) from $H_{eff} = -\lambda S_y^2$ to $H_{eff} = -\lambda(S_y^2 + \xi^2 S_x^2)$ [25] since the coupling between the states $|\downarrow\downarrow\rangle, |\uparrow\uparrow\rangle$ is proportional to $2\Omega_b\Omega_r = 2\Omega^2(1 - \xi^2)$ whereas the coupling between $|\downarrow\uparrow\rangle, |\uparrow\downarrow\rangle$ is proportional to $\Omega_b^2 + \Omega_r^2 = 2\Omega^2(1 + \xi^2)$. However, as long as $\xi \ll 1$ holds – which is the case in the experiments described in the next section – this effect is extremely small as the additional term is only quadratic in ξ .

Another side effect of setting $\xi \neq 0$ is the occurrence of an additional term $\propto S_z a^\dagger a$ in the Hamiltonian. It is caused by AC-Stark shifts arising from coupling to the upper and lower motional sideband which no longer completely cancel each other. The resulting shift of the qubit transition frequency depends on the vibrational quantum number n and is given by $\delta^{(SB)} = (8\eta^2\Omega^2/\epsilon)\xi n = (\epsilon/2)\xi n$. Simulations of the gate action based on (2) including an additional term $\propto S_z$ accounting for AC-Stark shifts of the dipole transitions and power-imbalanced beams show that the unwanted term $\propto S_z a^\dagger a$ has no severe effects for ions prepared in the motional ground state as long as $\xi \ll 1$. However, for ions in Fock states with $n > 0$, this is not the case. Taking the parameter set $\xi = 0.05$, $\nu = (2\pi) 1230$ kHz, and $\epsilon = (2\pi) 20$ kHz as an example, the following results are obtained: applying the gate to ions prepared in $|\downarrow\downarrow\rangle|n = 0\rangle$, a Bell state is created with fidelity 0.9996. For $n = 1$, the fidelity drops to 0.992, and for $n = 2$ to even 0.976. This loss of fidelity can be only partially recovered by shifting the laser

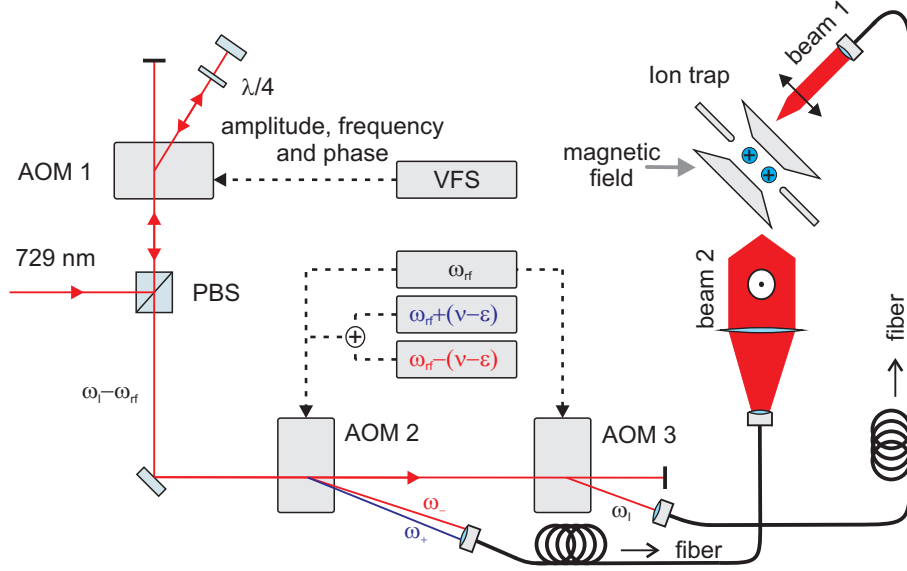


Figure 3. Trap geometry and optical qubit light field generation. AOM 1 controls the overall frequency ω_l and the amplitude of the laser beams at 729 nm. AOM 2 is used to switch beam 2 which illuminates both ions simultaneously. When supplied with two frequencies $\omega_{\text{rf}} \pm \delta$ where $\omega_{\text{rf}}/(2\pi) = 80$ MHz, it creates a bichromatic light field in the first order of diffraction. AOM 3 switches beam 1 which addresses only one of the ions. Both beams are guided with single mode optical fibers to the trap. The geometric alignment of polarizations, trap axis and magnetic field is as sketched. Radio-frequency signals supplying the AOMs are indicated as dotted lines.

frequency by $\delta^{(\text{SB})}$, the resulting fidelity being 0.996 and 0.988, respectively. For higher motional states, the effect is even more severe and shows that this kind of AC-Stark compensation is inappropriate when dealing with ions in a thermal state of motion with $\bar{n} \gg 1$. Instead of compensating the AC-Stark shift by imbalancing the beam powers, in this case, the laser frequency needs to be adjusted accordingly.

3. Experimental setup

Two $^{40}\text{Ca}^+$ ions are stored in a linear Paul trap with an axial trap frequency $\nu/(2\pi) = 1.232$ MHz corresponding to an inter-ion distance of $5 \mu\text{m}$. The $^{40}\text{Ca}^+$ optical qubit consists of the metastable state $|\uparrow\rangle = |D_{5/2}, m = 3/2\rangle$ with a lifetime of 1.17 s and the ground state $|\downarrow\rangle = |S_{1/2}, m = 1/2\rangle$ (see figure 1(b)). These two energy levels are connected via a quadrupole transition at a wavelength of 729 nm. Laser light at 397 nm is used for Doppler-cooling and state detection on the $S_{1/2} \leftrightarrow P_{1/2}$ transition with an additional repumping laser at 866 nm on the $D_{3/2} \leftrightarrow P_{1/2}$ transition. Fluorescence light is detected by means of a photomultiplier tube. For two ions we discriminate between $|\uparrow\uparrow\rangle$, $\{|\uparrow\downarrow\rangle \text{ or } |\downarrow\uparrow\rangle\}$ and $|\downarrow\downarrow\rangle$, the populations of which are labeled by p_0 , p_1 , and p_2 according to the number of ions fluorescing.

A titanium sapphire laser [26], whose frequency is stabilized to a high finesse Fabry-Perot cavity [27], is used to excite the quadrupole transition for sideband-

cooling, frequency-resolved optical pumping and performing quantum logic operations. Frequency drifts of maximally 3 Hz/s induced by the reference cavity are canceled by an automated measurement routine referencing the laser frequency to the optical qubit transition frequency and detecting the magnitude of the magnetic field at the ions' location of about 4 Gauss.

The setup for controlling the laser driving the qubit transition is depicted in figure 3. Laser light of 729 nm is sent to the ions from either of two directions, each beam having a maximum light power of 50 mW. Only when single-ion addressing is required we use laser beam 1 focused to a beam waist of $3 \mu\text{m}$ at the trap center with a k -vector perpendicular to the trap axis and a polarization that couples to all possible transitions. All other operations are accomplished with laser beam 2 whose k -vector encloses a 45° angle with the axis of the ion string and is perpendicular to the quantization axis defined by the direction of the magnetic field. With a beam waist of $14 \mu\text{m}$ at the trap center, this beam is adjusted to illuminate both ions with equal intensity. The polarization of this beam is set such that the coupling is maximal for $\Delta m = \pm 1$ transitions whereas it vanishes for all other transitions. The amplitude, frequency and phase of both beams is controlled by the acousto-optical modulator (AOM) 1 which is driven by a versatile frequency source (VFS). Amplitude pulse shaping is achieved with a variable gain amplifier controlled by a field programmable gate array. All radio-frequency sources are phase-locked to an ultra-stable quartz oscillator. By triggering each experimental cycle to the AC-power line we largely reduce distortions caused by the 1 mG magnetic field fluctuations at 50 Hz.

The AOMs 2 and 3 are used as switches for laser beams 1 and 2 applied from different directions. The bichromatic light field with frequencies $\omega_{\pm} = \omega_0 \pm \delta/(2\pi)$ is created by driving AOM 2 simultaneously with the two frequencies $\omega_{\text{rf}} \pm \delta$, where $\delta = \nu - \epsilon$. A frequency difference of $2\delta/(2\pi) = 2.4 \text{ MHz}$ leads to a diffraction into slightly different directions with an angular separation as small as 0.025° such that the coupling efficiency to the single mode fiber is reduced by about 15% compared to a single frequency beam where AOM 2 is driven with ω_{rf} . To generate the collective $\pi/2$ -pulses needed for analyzing the gate action, AOM 2 is driven with a single frequency ω_{rf} . A more detailed description of the apparatus is given in [4].

4. Measurement results

The coupling strength of the laser to the qubit is calibrated by recording resonant Rabi oscillations on the qubit transition. In case of short gate operations, the large intensities lead to big AC-Stark shifts and saturation of the gate coupling strength [12] which in turn necessitate a fine-adjustment of the laser frequency and power.

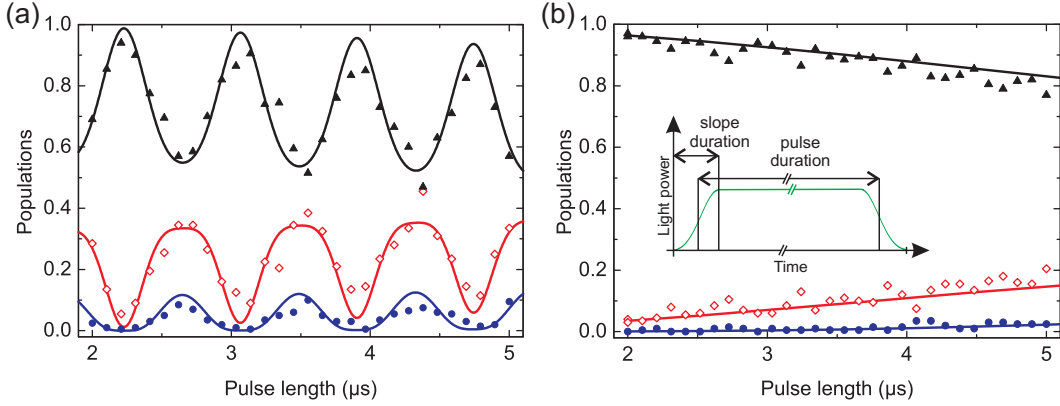


Figure 4. Effect of amplitude pulse shaping on non-resonant population transfer caused by a bichromatic light field non-resonantly exciting the carrier transition. Experimental results are presented for a gate duration of $t_{\text{gate}} = 25 \mu\text{s}$. A comparison of the evolution of the populations p_0 (\blacktriangle), p_1 (\diamond), p_2 (\bullet) for a square-shaped pulse (a) with an amplitude-shaped pulse (b) shows a suppression of the strong non-resonant oscillations for the latter case. The slopes are shaped as a Blackman window with a duration of $2.5 \mu\text{s}$, the figure inset showing the definitions of pulse and slope duration. Numerical simulations suggest that the actual pulse shape is not so important as long as the switching occurs sufficiently slowly. The solid lines are calculated from (9) and (4).

4.1. Amplitude pulse shaping

The merits of amplitude pulse shaping were studied by observing the time evolution of the populations p_i at the beginning of the gate operation when the population transfer is dominated by fast non-resonant coupling to the carrier. Figure 4 (a) shows the population evolution for the first $5 \mu\text{s}$ of a $25 \mu\text{s}$ gate operation based on a rectangular pulse shape. Averaging over a randomly varying phase ζ , we observe strong oscillations with a period of $2\pi/\delta = 0.84 \mu\text{s}$. Panel (b) shows that the non-resonant excitations vanish completely after application of amplitude pulse shaping with a slope duration of $2.5 \mu\text{s}$ corresponding to three vibrational periods of the center-of-mass mode. The slopes were shaped as a Blackman window [28], where the form of the shape is chosen such that a shaped and a rectangular pulse of the same duration have the same pulse area (see inset of panel (b)). Different pulse lengths are achieved by varying the duration of the central time interval during which the laser power is constant. The solid lines in the figure are calculated from (9) and (4) and fit the data well.

4.2. AC-Stark shift compensation

The AC-Stark shift caused by bichromatic light with spectral components each having a Rabi frequency of $\Omega/(2\pi) = 220 \text{ kHz}$ (for $t_{\text{gate}} = 25 \mu\text{s}$) is measured by scanning the global laser frequency using AOM 1. The resulting populations after a gate operation are depicted in figure 5 (a). We observe a drop of the population p_1 to zero at a detuning of $(2\pi) 37 \text{ kHz}$ from the carrier transition. At this setting the ions are maximally entangled.

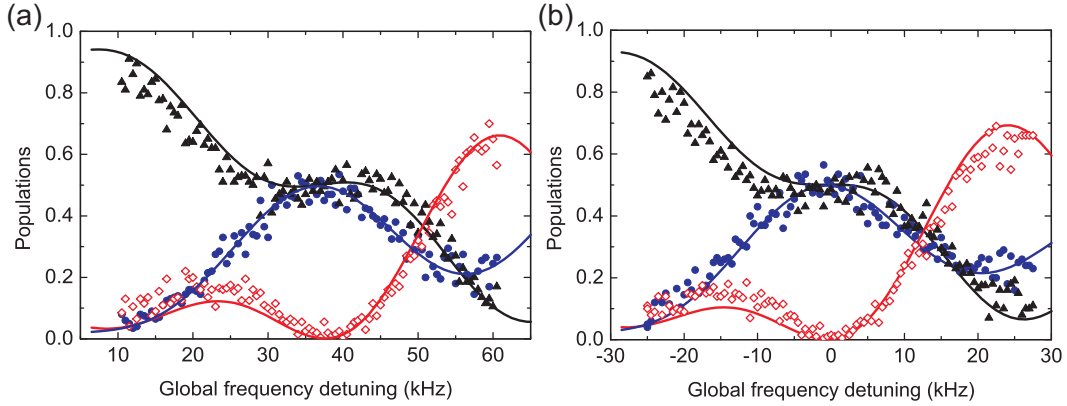


Figure 5. (a) Populations p_0 (\blacktriangle), p_1 (\diamond), p_2 (\bullet) after a single gate operation ($t_{\text{gate}} = 25 \mu\text{s}$) where the global frequency detuning of the bichromatic entangling pulse is varied by scanning AOM 1. A maximally entangled state is achieved for a global frequency detuning of $(2\pi)37 \text{ kHz}$ relative to the qubit transition frequency due to AC-Stark shifts. (b) Introduction of a beam imbalance $\xi = 0.08$ shifts the pattern of the populations by the required amount to fully compensate for the AC-Stark-shift (note the different x-axis offsets in (a) and (b)). The solid lines are calculated by solving the Schrödinger equation for the Hamiltonian given in (2) amended by a term accounting for the measured AC-Stark shift.

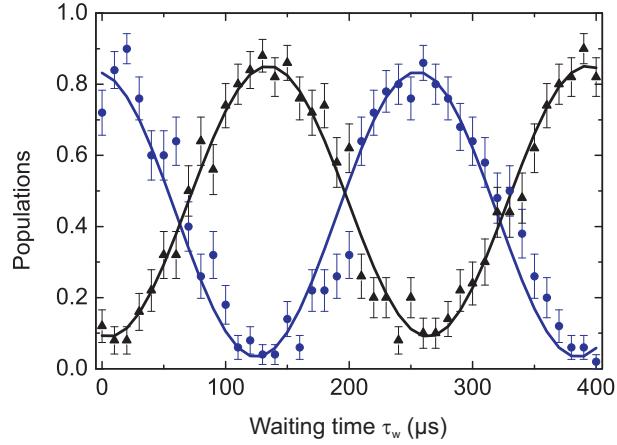


Figure 6. Population evolution of $|\uparrow\uparrow\rangle$ (\bullet) and $|\downarrow\downarrow\rangle$ (\blacktriangle) when scanning the waiting time between two $25 \mu\text{s}$ gate pulses in a Ramsey-like experiment. For this scan the detuning ϵ was set to $(2\pi)40 \text{ kHz}$. In this set of data, the AC-Stark shift was only partially compensated by imbalancing the power of the two frequency components. From the sinusoidal fits shown as solid lines, we infer an oscillation period of $258(4) \mu\text{s}$ corresponding to a residual AC-Stark shift of $(2\pi)1.94(3) \text{ kHz}$.

By changing the relative power of the bichromatic field's frequency components such that $\xi = 0.08$ the AC-Stark shift is compensated. This translates the whole excitation pattern in frequency space as can be seen in figure 5 (b).

A more sensitive method to infer the remaining AC-Stark shift δ_{AC} after a coarse pre-compensation consists in concatenating two gates separated by a waiting time τ_w in a pulse sequence akin to a Ramsey-type experiment [29] and scanning τ_w . This

procedure maps δ_{AC} to a phase $\phi = \delta_{AC}\tau_w$ which is converted into a population change $p_2 = \cos^2(\phi)$, $p_0 = \sin^2(\phi)$ by the second gate pulse. For two ions, the corresponding Ramsey pattern displayed in figure 6 shows oscillations of the populations p_0 and p_2 with a frequency of two times the remaining AC-Stark shift.

4.3. Gate analysis

A full characterization of the gate operation could be achieved by quantum process tomography [30]. At present, however, the errors introduced by single ion addressing and individual qubit detection are on the few percent level in our experimental setup which renders the detection of small errors difficult in the entangling operation. Instead, we characterize the quality of the gate operation by using it for creating different Bell states and determining their fidelities.

For the Bell state $\Psi_1 = |\downarrow\downarrow\rangle + i|\uparrow\uparrow\rangle$, the fidelity is given by $F = \langle\Psi_1|\rho^{\text{exp}}|\Psi_1\rangle = (\rho_{\uparrow\uparrow,\uparrow\uparrow}^{\text{exp}} + \rho_{\downarrow\downarrow,\downarrow\downarrow}^{\text{exp}})/2 + \text{Im}\rho_{\downarrow\downarrow,\uparrow\uparrow}^{\text{exp}}$, with the density matrix ρ^{exp} describing the experimentally produced state. To determine F , we need to measure the populations $p_2 + p_0$ at the end of the gate operation as well as the off-diagonal matrix-element $\rho_{\downarrow\downarrow,\uparrow\uparrow}^{\text{exp}}$. To determine the latter, we apply a $\pi/2$ pulse with optical phase ϕ to both ions and measure $\langle\sigma_z^{(1)}\sigma_z^{(2)}\rangle$ for the resulting state as a function of ϕ . This procedure is equivalent to measuring oscillations of the expectation value $\text{Tr}(P(\phi)\rho^{\text{exp}})$ of the operator $P(\phi) = \sigma_\phi^{(1)}\sigma_\phi^{(2)}$ where $\sigma_\phi = \sigma_x \cos \phi + \sigma_y \sin \phi$ (see figure 9 (b) and (d)). The amplitude A of these oscillations equals $2|\rho_{\downarrow\downarrow,\uparrow\uparrow}^{\text{exp}}|$ and is obtained by fitting them with the function $P_{\text{fit}}(\phi) = A \sin(2\phi + \phi_0)$.

Previous measurements [9] using $|\downarrow\downarrow\rangle$ as input state have demonstrated Bell state fidelities as high as 0.993(1) (see figure 9 (a) and (b)) for gate times of 50 μs or 61 trap oscillation periods. By doubling the detuning to $\epsilon/(2\pi) = 40$ kHz we reduce the gate duration to only 31 trap oscillation periods and observe Bell states with a fidelity of 0.971(2) which is remarkable considering the small Lamb-Dicke parameter of $\eta = 0.044$. The detrimental effects illustrated in figure 4 (a) are sufficiently suppressed by amplitude pulse shaping.

Moreover, for a gate time of 50 μs the analysis was extended by applying the gate to the state $|\downarrow\uparrow\rangle$ which is prepared by a $\pi/2$ rotation (beam 2) of both ions, followed by a π phase shift pulse on a single ion performed with the far-detuned focused beam 1, and another $\pi/2$ rotation applied to both ions. This pulse sequence realizes the mapping

$$|\downarrow\downarrow\rangle \longrightarrow |\downarrow + \uparrow\rangle|\downarrow + \uparrow\rangle \longrightarrow |\downarrow - \uparrow\rangle|\downarrow + \uparrow\rangle \longrightarrow |\downarrow\uparrow\rangle \quad (10)$$

to the desired input state for the gate. Imperfections of single-ion addressing lead to an error in state preparation of 0.036(3). For the Bell state analysis, we measure the population p_1 to infer $\rho_{\downarrow\downarrow,\downarrow\downarrow}^{\text{exp}} + \rho_{\uparrow\uparrow,\uparrow\uparrow}^{\text{exp}}$. Unfortunately parity oscillations cannot be introduced by a collective $\pi/2$ pulse acting on the state $|\uparrow\downarrow\rangle + i|\downarrow\uparrow\rangle$. Instead, we transform this state into $|\uparrow\uparrow\rangle + i|\downarrow\downarrow\rangle$ by repeating the steps of sequence (10) as for the state preparation and measure again the coherence by performing parity oscillations.

Figure 7 shows a comparison of the fidelity of the gate starting either in $|\downarrow\downarrow\rangle$ or $|\downarrow\uparrow\rangle$. The fidelity of a Bell state created by a single gate starting in $|\downarrow\uparrow\rangle$ is 0.95(1). Taking

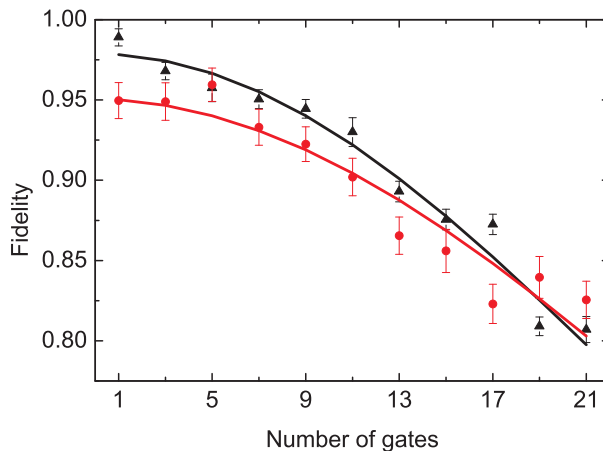


Figure 7. Bell state fidelities after gate operations applied to the input states $|\downarrow\downarrow\rangle$ (▲) and $|\downarrow\uparrow\rangle$ (●) for $t_{\text{gate}} = 50\mu\text{s}$. Taking into account the error for state preparation of the input states $|\downarrow\uparrow\rangle$ and a similar error to measure the parity signal, we conclude that the gate operation works on all tested input states similarly well. The solid lines reflect a Gaussian decay of the parity fringe amplitudes as a function of the number of gates and a linear decay in the desired populations caused by the spectral impurity of the laser. For both input states the gate operation implies errors of less than 0.2 after 21 consecutive applications.

into account the errors for state preparation and the Bell state analysis we conclude that the entangling operation works equally well for $|\downarrow\uparrow\rangle$ as an input state. This hypothesis is supported by the observation that for both states we obtain a similar decay of Bell state fidelities with increasing gate number.

Compared with our earlier results [9] where multiple gate operations were induced by varying the duration of a single bichromatic pulse, here we applied up to 21 individual amplitude-shaped pulses. Splitting up a long pulse into many shorter gate pulses has no detectable effect on the fidelity of the Bell states produced, and in both cases we obtain a Bell state fidelity larger than 0.80 after 21 gates.

4.4. Gate errors

As discussed in [9], the two dominant sources of gate errors are laser frequency noise and variations of the laser-ion coupling strength. Imperfections of the laser's frequency spectrum lead to incoherent carrier excitation and thus to a loss in the Bell state fidelity of 2×10^{-3} per gate. Coupling strength variations of $\delta\Omega/\Omega \approx 1.4(1) \times 10^{-2}$ are the major cause for the Gaussian decay of the parity oscillation amplitudes.

An error that was not investigated in detail before is the dependence of the Bell state fidelity on the global laser frequency detuning from the qubit transition frequency. Experimental results are shown in figure 8. The solid line fitting the data is calculated by numerically solving the full Schrödinger equation for different global frequency detunings and evaluating the fidelity. A second order frequency dependence of $-9.6(3) \times 10^{-9} \text{ Hz}^2$ is found from calculations at the maximum point. This suggests that our laser's typical

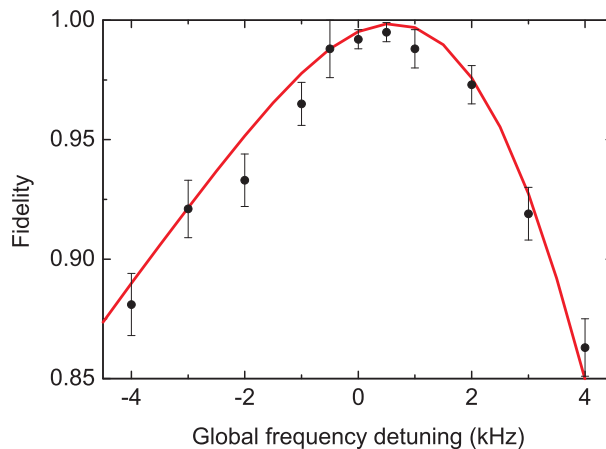


Figure 8. Fidelity as a function of the global frequency detuning of the bichromatic light pulse for from the carrier transition (here, the sideband detuning was set to $\epsilon/(2\pi) = 20$ kHz). A maximum fidelity of 0.995(4) was found for a detuning of 500 Hz from the transition center due to a residual AC-Stark shift. The solid line is obtained by numerically solving equation (2) and taking into account the AC-Stark shift compensation by different powers of the blue and the red laser frequency component. At the maximum, the solid line experiences a second order frequency dependence of $-9.6(3) \times 10^{-9} \text{ Hz}^2$.

mean frequency deviation of 160 Hz contributes with 3×10^{-4} to the error budget.

A further error source arises when the bichromatic beam couples to both ions with different strengths. By recording Rabi oscillations simultaneously on the two ions we conclude that both ions experience the same coupling strength Ω to within 4%. From numerical calculations we infer an additional error in the measured Bell state fidelity of less than 1×10^{-4} .

Another possible error source is heating of the COM-mode during the gate operation since the gate is not insensitive to motional heating in the parameter regime of our implementation. Using the calculation performed in [21], we find a fidelity reduction of $\Delta F = \Gamma_h t_{\text{gate}}/2$ where Γ_h is the heating rate of the COM-mode. As in our experiments $\Gamma_h = 3s^{-1}$, the fidelity is reduced by $\Delta F \approx 10^{-4}$ for $t_{\text{gate}} = 50 \mu\text{s}$.

5. A Mølmer-Sørensen gate with ions in a thermal state of motion

5.1. Formal description of the time evolution

In theory, the Mølmer-Sørensen gate does not require the ions to be cooled to the ground states of motion since its propagator (4) is independent of the vibrational state for $t = t_{\text{gate}}$. For $t \neq t_{\text{gate}}$, however, the interaction entangles qubit states and vibrational states so that the qubits' final state becomes dependent on the initial vibrational state. Therefore, it is of interest to calculate expectation values of observables acting on the qubit state space after applying the propagator for an arbitrary time t . As will be shown below, simple expressions can be derived in the case of a thermally occupied

motional state. For the following calculation, it is convenient to define $V(t) = \exp(i\gamma S_y^2)$ where $\gamma = \lambda t - \chi \sin(\epsilon t)$. We are interested in calculating the expectation value of the observable \mathcal{O} given by

$$\begin{aligned} O(t) &= \text{Tr}(\mathcal{O}U(t)\rho_M \otimes \rho_A U(t)^\dagger) \\ &= \text{Tr}(\rho_M \otimes \rho_A \hat{D}(-\alpha S_y) V^\dagger \mathcal{O} V \hat{D}(\alpha S_y)) \\ &= \sum_n p_n \text{Tr}_A(\rho_A \langle n | \hat{D}(-\alpha S_y) V^\dagger \mathcal{O} V \hat{D}(\alpha S_y) | n \rangle). \end{aligned} \quad (11)$$

Here, $\rho_M = \sum_n p_n |n\rangle\langle n|$ with $p_n = \frac{1}{\bar{n}+1} \left(\frac{\bar{n}}{\bar{n}+1}\right)^n$ describes a thermal state with average phonon number \bar{n} and Tr_A denotes the trace over the qubit state space with ρ_A being the initial state of the qubits. For two ions, the state-dependent displacement operator $\hat{D}(\alpha S_y)$ is given by

$$\hat{D}(\alpha S_y) = P_0 + P_2 \hat{D}(2\alpha) + P_{-2} \hat{D}(-2\alpha),$$

where P_λ is the projector onto the space spanned by the eigenvectors of S_y having the eigenvalue λ , with $P_0 = \mathbb{1} - \frac{1}{4}S_y^2$, and $P_{\pm 2} = \frac{1}{8}(S_y^2 \pm 2S_y)$. This decomposition allows for tracing over the vibrational states in (11) since $\langle n | \hat{D}(\alpha) | n \rangle = \exp(-|\alpha|^2/2) \mathcal{L}_n(|\alpha|^2)$, where \mathcal{L}_n denotes a Laguerre polynomial. For taking the trace, we note that $\sum_n p_n \langle n | \hat{D}(\alpha) | n \rangle$ is proportional to the generating function $g(x, \beta)$ of the Laguerre polynomial [31] given by

$$g(x, \beta) = \sum_{n=0}^{\infty} \mathcal{L}_n(\beta) x^n = \frac{1}{1-x} \exp\left(-\frac{\beta x}{1-x}\right).$$

Therefore,

$$\sum_n p_n \langle n | \hat{D}(\alpha) | n \rangle = \frac{1}{\bar{n}+1} g\left(\frac{\bar{n}}{\bar{n}+1}, |\alpha|^2\right) \exp(-|\alpha|^2/2) = e^{-|\alpha|^2(\bar{n}+\frac{1}{2})}. \quad (12)$$

Using the abbreviation $\mathcal{O}_V = V \mathcal{O} V^\dagger$ and (12), the expectation value $O(t)$ is given by

$$O(t) = \text{Tr}_A(\mathcal{O}_V \{A_0 + A_4 e^{-4|\alpha|^2(\bar{n}+\frac{1}{2})} + A_{16} e^{-16|\alpha|^2(\bar{n}+\frac{1}{2})}\}) \quad (13)$$

with

$$\begin{aligned} A_0 &= P_0 \rho_A P_0 + P_2 \rho_A P_2 + P_{-2} \rho_A P_{-2} \\ A_4 &= P_2 \rho_A P_0 + P_0 \rho_A P_2 + P_{-2} \rho_A P_0 + P_0 \rho_A P_{-2} \\ A_{16} &= P_{-2} \rho_A P_2 + P_2 \rho_A P_{-2}. \end{aligned}$$

For the initial state $\rho_A = |\downarrow\downarrow\rangle\langle\downarrow\downarrow|$, one obtains

$$A_0 = (S_z^2 + S_x^2)/16, \quad A_4 = -S_z/4, \quad A_{16} = (S_z^2 - S_x^2)/16$$

and

$$O(t) = \frac{1}{16} \text{Tr}_A(\mathcal{O}_V \{(S_z^2 + S_x^2) - 4S_z e^{-4|\alpha|^2(\bar{n}+\frac{1}{2})} + (S_z^2 - S_x^2) e^{-16|\alpha|^2(\bar{n}+\frac{1}{2})}\}).$$

To calculate the time evolution of the qubit state populations starting from state $|\downarrow\downarrow\rangle$ at $t = 0$, use of the relations

$$\begin{aligned} e^{-i\gamma S_y^2} S_z e^{i\gamma S_y^2} &= \cos(4\gamma) S_z - \sin(4\gamma) \frac{1}{2} \{S_x, S_y\} \\ e^{-i\gamma S_y^2} S_j^2 e^{i\gamma S_y^2} &= S_j^2 \end{aligned}$$

yields the following expressions for the qubit state populations:

$$\begin{aligned}
 p_2(t) &= \frac{1}{8}(3 + e^{-16|\alpha|^2(\bar{n}+\frac{1}{2})} + 4 \cos(4\gamma)e^{-4|\alpha|^2(\bar{n}+\frac{1}{2})}) \\
 p_1(t) &= \frac{1}{4}(1 - e^{-16|\alpha|^2(\bar{n}+\frac{1}{2})}) \\
 p_0(t) &= \frac{1}{8}(3 + e^{-16|\alpha|^2(\bar{n}+\frac{1}{2})} - 4 \cos(4\gamma)e^{-4|\alpha|^2(\bar{n}+\frac{1}{2})})
 \end{aligned}
 \tag{14}$$

The formalism presented here could also be used to calculate the contrast of a parity scan for thermal states of motion. In this case, the parity operator is given by $P = S_z^2/2 - \mathbb{1}$. The $\pi/2$ carrier pulses transform this operator into an operator $P_\phi = (\cos \phi S_x + \sin \phi S_y)^2/2 - \mathbb{1}$.

5.2. High fidelity Bell states of ions in a thermal state

While many theoretical papers discussing Mølmer-Sørensen and conditional phase gates put much emphasis on the possibility of entangling ions irrespective of their motional state by using these gates, there has not been any experimental demonstration of this gate property up to now. The reason for this is that independence of the motional state, as predicted by (4), is achieved only deep within the Lamb-Dicke regime whereas experiments demonstrating entangling gates on hyperfine qubits usually have Lamb-Dicke factors on the order of $\eta = 0.1 - 0.2$ [10, 8, 32]. Therefore, all previous experimental gate realizations used laser cooling to prepare at least the motional mode mediating the gate in its ground state with $n = 0$.

Figure 9 (a) illustrates the population evolution induced by the gate pulse for ground-state cooled ions initially prepared in the qubit states $|\downarrow\downarrow\rangle$, figure 9 (b) displays parity oscillations for the produced Bell state. The corresponding time evolution and parity oscillations for ions that are merely Doppler-cooled to a thermal state with $\bar{n} = 20(2)$ are shown in figure 9 (c) and (d) respectively. As the coupling strengths on the upper and lower motional sidebands scale as $\propto \sqrt{n+1}$ and $\propto \sqrt{n}$, non-resonant sideband excitation transfers population much faster from $|\downarrow\downarrow, n\rangle$ into $|\downarrow\uparrow, n \pm 1\rangle$, $|\uparrow\downarrow, n \pm 1\rangle$ as compared to the case of ions prepared in the ground state with $\bar{n} = 0$. After the gate time $t_{\text{gate}} = 50 \mu\text{s}$, however, the undesired population p_1 nearly vanishes as in the case of ground-state cooled ions and the Bell state Ψ_1 is again created. In the experiment, we find a population $p_1 = 0.015(1)$ in the undesired energy eigenstates. The parity oscillations have an amplitude of 0.964(2), resulting in a Bell state fidelity of 0.974(1). The reasons for the somewhat reduced fidelity as compared with ground-state cooled ions are currently not well understood. In part, the fidelity loss arises from a variation of the coupling strength on the vibrational sidebands as a function of n caused by higher-order terms in η . However, for a thermal state with $\bar{n} = 20$ and $\eta = 0.044$ calculations show this effect amounts only to additional errors of 7×10^{-3} .

As mentioned in Section 2.2, the AC-Stark compensation by unbalancing the power of the red and blue frequency component is not applicable to ions in a thermal state. Instead, the laser frequency needs to be adjusted to account for AC-Stark shifts δ_{AC} , a

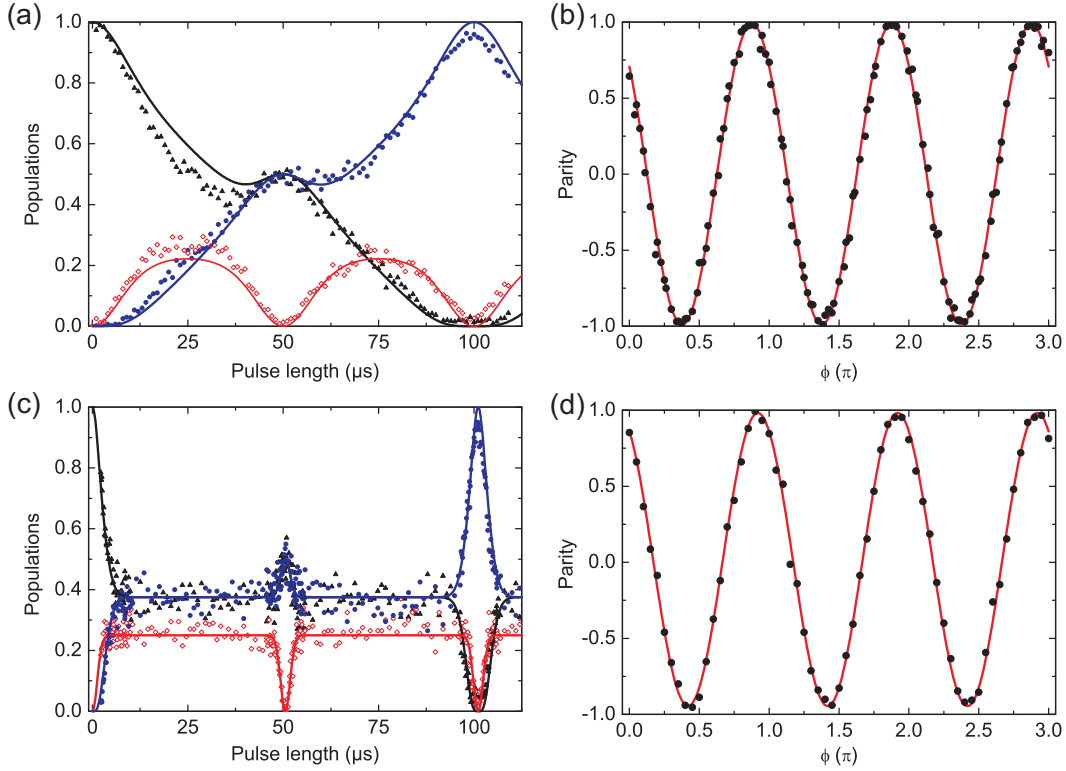


Figure 9. Measured population evolution for p_0 (\blacktriangle), p_1 (\diamond), p_2 (\bullet) and parity oscillations with (a,b) and without (c,d) ground state cooling. In the latter case, population is transferred faster into $|\uparrow\downarrow, n\rangle$, $|\downarrow\uparrow, n\rangle$ as compared to sideband cooled ions due to the higher coupling strength to the sidebands. In (c), the solid lines are a fit to the data points using (14) with the mean phonon number \bar{n} as a free parameter giving $\bar{n} = 20(2)$. The parity oscillations for the ions in a thermal state of motion have an amplitude of $0.964(2)$. Combining both measurements, we determine the Bell state fidelity to be $0.974(1)$. The data appearing in (a) and (b) are taken from [9]. Here the deviation of the solid lines from the data is caused by the AC-Stark shift compensation using $\zeta = 0.08$.

technique that works well as long as the AC-Stark shifts are smaller than the coupling strength λ of the gate interaction appearing in (5) (otherwise, in the case $\delta_{AC} \gg \lambda$, small laser power fluctuations give rise to large phase shifts). Therefore, care must be taken to choose the direction and polarization of the gate laser such that a favorable ratio λ/δ_{AC} is obtained. In experiments with a gate duration of $t_{\text{gate}} = 50 \mu\text{s}$, we achieved $\lambda/\delta_{AC} \approx 3$ and needed to shift the laser frequency by about 7.5 kHz for optimal Bell state fidelity. In future experiments, a further reduction of the AC-Stark shift could be obtained using a σ^+ -polarized laser beam incident on the ions along the direction of the magnetic field. In this geometry the AC-Stark shift is predominantly caused by the $S_{1/2} \leftrightarrow P_{3/2}$ dipole transition since the $D_{5/2}(m = +3/2)$ state does not couple to any of the 4p Zeeman states. From calculations we infer a reduction of the shift to about 2 kHz without compromising the gate speed.

Fitting equations (14) to the population evolution data allows us to determine

the mean vibrational quantum number as $\bar{n} = 20(2)$. This value is consistent with independent measurements obtained by comparing the time evolution of the ions when exciting them on the carrier and on the blue motional sideband.

6. Conclusions and outlook

Until recently, entangling gates for optical qubits were exclusively of the Cirac-Zoller type which require individual addressing of the ions. Compared to this type of gate the Mølmer-Sørensen gate gives an improvement in fidelity and speed of nearly an order of magnitude. The achieved fidelity sets a record for creating two-qubit entanglement on demand irrespective of the physical realization considered so far. Our results with concatenations of 21 of these operations bring the realization of more complex algorithms a step closer to reality. The implementation of a gate without the need for ground state cooling is of particular interest in view of quantum algorithms that require entangling gates conditioned on quantum state measurements that do not preserve the ions' motional quantum state.

The optical qubit as used here is certainly not the best solution for long time storage of quantum information. Instead, qubits encoded in two hyperfine ground states whose frequency difference is insensitive to changes in magnetic field are preferable. These magnetic-field insensitive hyperfine qubits can store quantum information for times exceeding the duration of the gate operation presented here by more than four orders of magnitude [2, 3, 4]. However, on such qubit states no high-fidelity universal gates have been demonstrated so far. Hence, our next experimental efforts will focus on implementing the Mølmer-Sørensen gate using $^{43}\text{Ca}^+$ ions. By mapping between the hyperfine qubit encoded in the ion's ground states and the optical qubit we will benefit from both of their advantages.

Another interesting perspective of this gate is to create multi-qubit interactions between more than two qubits. A gate collectively interacting with all ions at the same time, in combination with a collective spin flips and a strongly focused off-resonant laser beam inducing phase shifts in individual ions, constitutes a basis set of Hamiltonians that offers the prospect of realizing complex multi-qubit operations such as a Toffoli-gate and a quantum error-correcting algorithm [33].

Acknowledgments

We gratefully acknowledge the support of the European network SCALA, the Institut für Quanteninformation GmbH and IARPA. R. G. acknowledges funding by the Marie-Curie program of the European Union (grant number PIEF-GA-2008-220105).

References

- [1] DiVincenzo D P 2000 *Fortschr. Phys.* **48** 771

- [2] Langer C, Ozeri R, Jost J D, Chiaverini J, Demarco B, Ben-Kish A, Blakestad R B, Britton J, Hume D B, Itano W M, Leibfried D, Reichle R, Rosenband T, Schaetz T, Schmidt P O and Wineland D J 2005 *Phys. Rev. Lett.* **95** 060502
- [3] Olmschenk S, Younge K C, Moehring D L, Matsukevich D N, Maunz P and Monroe C 2007 *Phys. Rev. A* **76** 052314
- [4] Benhelm J, Kirchmair G, Roos C F and Blatt R 2008 *Phys. Rev. A* **77** 062306
- [5] Roos C F, Chwalla M, Kim K, Riebe M and Blatt R 2006 *Nature* **443** 316
- [6] Myerson A H, Szwer D J, Webster S C, Allcock D T C, Curtis M J, Imreh G, Sherman J A, Stacey D N, Steane A M and Lucas D M 2008 *Phys. Rev. Lett.* **100** 200502
- [7] Knill E, Leibfried D, Reichle R, Britton J, Blakestad R B, Jost J D, Langer C, Ozeri R, Seidelin S and Wineland D J 2008 *Phys. Rev. A* **77** 012307
- [8] Leibfried D, DeMarco B, Meyer V, Lucas D, Barrett M, Britton J, Itano W M, Jelenković B, Langer C, Rosenband T and Wineland D J 2003 *Nature* **422** 412
- [9] Benhelm J, Kirchmair G, Roos C F and Blatt R 2008 *Nat. Phys.* **4** 463
- [10] Sackett C A, Kielpinski D, King B E, Langer C, Meyer V, Myatt C J, Rowe M, Turchette Q A, Itano W M, Wineland D J and Monroe C 2000 *Nature* **404** 256
- [11] Chiaverini J, Leibfried D, Schaetz T, Barrett M D, Blakestad R B, Britton J, Itano W M, Jost J D, Knill E, Langer C, Ozeri R and Wineland D J 2004 *Nature* **432** 602
- [12] Roos C F 2008 *New J. Phys.* **10** 013002
- [13] Steane A 1998 *Rep. Prog. Phys.* **61** 117
- [14] Rowe M A, Ben-Kish A, DeMarco B, Leibfried D, Meyer V, Beall J, Britton J, Hughes J, Itano W M, Jelenković B, Langer C, Rosenband T and Wineland D J 2002 *Quant. Inf. Comp.* **2** 257
- [15] Blinov B, Deslauriers L, Lee P, Madsen M, Miller R and Monroe C 2002 *Phys. Rev. A* **65** 040304
- [16] Barrett M D, DeMarco B, Schaetz T, Leibfried D, Britton J, Chiaverini J, Itano W M, Jelenković B, Jost J D, Langer C, Rosenband T and Wineland D J 2003 *Phys. Rev. A* **68** 042302
- [17] Lee P J, Brickman K A, Deslauriers L, Haljan P C, Duan L and Monroe C 2005 *J. Opt. B* **7** 371
- [18] Milburn G J, Schneider S and James D F 2000 *Fortschr. Phys.* **48** 801
- [19] Sørensen A and Mølmer K 1999 *Phys. Rev. Lett.* **82** 1971
- [20] Solano E, de Matos Filho R L and Zagury N 1999 *Phys. Rev. A* **59** R2539
- [21] Sørensen A and Mølmer K 2000 *Phys. Rev. A* **62** 022311
- [22] Häffner H, Gulde S, Riebe M, Lancaster G, Becher C, Eschner J, Schmidt-Kaler F and Blatt R 2003 *Phys. Rev. Lett.* **90** 143602
- [23] James D F V 1998 *Appl. Phys. B* **66** 181
- [24] Schmidt-Kaler F, Häffner H, Gulde S, Riebe M, Lancaster G P T, Deuschle T, Becher C, Hänsel W, Eschner J, Roos C F and Blatt R 2003 *Appl. Phys. B* **77** 789
- [25] Unanyan R G and Fleischhauer M 2003 *Phys. Rev. Lett.* **90** 133601
- [26] Benhelm J, Kirchmair G, Rapol U, Körber T, Roos C F and Blatt R 2007 *Phys. Rev. A* **75** 032506
- [27] Notcutt M, Ma L S, Ye J and Hall J L 2005 *Opt. Lett.* **30** 1815
- [28] Harris F J 1978 *Proc. IEEE* **66** 51
- [29] Leibfried D, Barrett M D, Schaetz T, Britton J, Chiaverini J, Itano W M, Jost J D, Langer C and Wineland D J 2004 *Science* **304** 1476
- [30] Riebe M, Kim K, Schindler P, Monz T, Schmidt P O, Körber T K, Hänsel W, Häffner H, Roos C F and Blatt R 2006 *Phys. Rev. Lett.* **97** 220407
- [31] Abramowitz M and Stegun I A 1972 *Handbook of mathematical functions* (New York: Dover) p. 784
- [32] Haljan P C, Lee P J, Brickman K A, Acton M, Deslauriers L and Monroe C 2005 *Phys. Rev. A* **72** 062316
- [33] Nebendahl V, Häffner H and Roos C F 2008 arXiv:0809.1414